Vibration Signature Analysis of High-Speed Unbalanced Rotors Supported by Rolling-Element Bearings due to Off-Sized Rolling Elements

Sanjay H. Upadhyay, Suraj P. Harsha, and S. C. Jain

Mechanical & Industrial Engineering Department, Indian Institute of Technology, Roorkee, India

(Received 28 August 2008; revised 21 April 2009; accepted 11 June 2009)

In this paper an analytical model has been developed to investigate the nonlinear dynamic behavior of an unbalanced rotor-bearing system due to ball size variation of the rolling elements. Two cases of ball-size variation were considered: variations of 0.2 micron and 2 microns. In the analytical formulation, the contact between rolling elements and inner/outer races was considered a nonlinear spring, which became stiff using the Hertzian elastic deformation theory. A detailed contact-damping model reflecting the influences of the surface profiles and the speeds of both contacting elements was developed and applied in the rolling-element bearing model. The mathematical formulation accounted for the sources of nonlinearity, such as the Hertzian contact force, varying speed, and radial internal clearance. The equations of motion of a rolling-element bearing were formulated in generalized coordinates, using Lagrange's equations that consider the vibration characteristics of the individual constituents, such as inner race, outer race, rolling elements, and shaft, in order to investigate the structural vibration of the bearing. All results have been presented in form of Fast Fourier Transformations (FFT) and Poincaré maps. The highest radial vibrations due to ball-size variation were at a speed of the number of balls multiplied by the cage speed ($\omega = k\omega_{\text{cage}}$ Hz). The other vibrations due to ball-size variation occurred at $VC \pm k\omega_{\text{cage}}$, where k was a constant. The current study provides a powerful tool for design and health monitoring of machine systems.

NOMENCLATURE

$F_{\text{d-in}}$ – roller-inner race contact damping force
$F_{\text{d-out}}$ – roller-outer race contact damping force
F_{u} – Unbalanced rotor force, N
k_{in} – equivalent non-linear contact stiffness of the roller-inner race contact
k_{out} – equivalent non-linear contact stiffness of the roller-outer race contact
$k_{\text{in-contact}}$ – contact stiffness of the roller-inner race contact
$k_{\text{out-contact}}$ – contact stiffness of the roller-outer race contact
c_{in} – equivalent viscous damping factor of the roller-inner race contact
c_{out} – equivalent viscous damping factor of the roller-outer race contact
I – moment of inertia of each rolling element
I_{cage} – moment of inertia of the cage
I_{in} – moment of inertia of the inner race
I_{out} – moment of inertia of the outer race
M_{in} – mass of the inner race, kg
M_{j} – mass of the rolling elements, kg
M_{out} – mass of the outer race, kg
M_{rotor} – mass of the rotor, kg
N_{b} – number of balls
R – radius of outer race
r – radius of inner race
r_{in} – position of mass centre of inner race
r_{out} – position of mass centre of outer race
T – kinetic energy of the bearing system
T_{cage} – kinetic energy of the cage
$T_{\text{i-race}}$ – kinetic energy of the inner race
$T_{\text{o-race}}$ – kinetic energy of the outer race
$T_{\text{r.e}}$ – kinetic energy of the rolling elements
V – potential energy of the bearing system
V_{cage} – potential energy of the cage
$V_{\text{i-race}}$ – potential energy of the inner race
$V_{\text{o-race}}$ – potential energy of the outer race
$V_{\text{r.e}}$ – potential energy of the rolling elements
V_{spring} – potential energy of the springs
$x_{\text{in}}, y_{\text{in}}$ – centre of inner race
$x_{\text{out}}, y_{\text{out}}$ – centre of outer race
$\delta_{\text{in}+}$ – contact deformation of the roller-inner race
$\delta_{\text{out}+}$ – contact deformation of the roller-outer race
$\left(\dot{\phi}\right)_{\text{in}}$ – angular velocity of inner race
$\left(\dot{\phi}\right)_{\text{in}}$ – angular velocity of outer race
δ – deformation at the point of contact at inner and outer race, mm
$\Delta\Gamma$ – diameter difference of the off-sized ball, μm
γ – internal radial clearance
λ – Lyapunov exponent
ω_{cage} – angular velocity of the cage, rad/s
ω_{inner} – angular velocity of the inner race, rad/s
ω_{outer} – angular velocity of the outer race, rad/s

ρ_j – radial position of the rolling element
ρ_r – radius of each rolling element
θ_j – angular position of rolling element
χ_j – position of j^{th} rolling element from the centre of inner race
VC – varying compliance frequency, Hz
X – rotational frequency, Hz
FFT – fast Fourier transformations

1. INTRODUCTION

Rolling-element bearings have widespread domestic and industrial applications. Proper functioning of the appliances depends, to a great extent, on the smooth and quiet running of the bearings. The defects in rolling-element bearings can be categorized as "local" or "distributed." The distributed defects in rolling-element bearings include surface roughness, waviness, misaligned races, and off-size rolling elements.[1–3] The surface features were considered in terms of wavelength compared to the Hertzian contact width of the rolling-element raceway contacts. Surface features of wavelength characterized by the contact width or less were termed "roughness," whereas longer wavelength features were termed "waviness."[3] Distributed defects are caused by manufacturing error, improper installation, or abrasive wear.[4] The variation in contact force between rolling elements and raceways due to the distributed defects resulted in increased vibration level.

Vibration produced by waviness was first studied by Tallian and Gustafsson.[1] It is generally known that a ball bearing may still cause vibrations even when it is defect-free.[5–7] Aktürk studied some characteristic parameters that affect the natural frequency of a rotating shaft supported by defect-free ball bearings.[8] The conclusion of this work shows that large values of axial preload causes stiffer spring characteristics and results in higher natural frequency values. Harsha et al. analyzed the nonlinear behavior of ball bearings due to the number of balls and the preload effect.[9] We found the nonlinear dynamic response to be associated with the ball-passage frequency. The amplitude of the vibration is considerably reduced if the number of balls and the preload are correctly selected.

For this paper, a theoretical investigation was conducted to observe the effect of ball-size variations on the nonlinear vibration characteristics of a rotor-bearing system. To determine how the nonlinear bearing forces act on the system, the implicit numerical integration technique Newmark-β with the Newton–Raphson method was used to solve the nonlinear differential equations iteratively.[16] The results obtained from a large number of numerical integrations are mainly presented in the form of a fast Fourier transformation and Poincaré maps.

2. PROBLEM FORMULATION

A schematic diagram of the rolling-element bearing is shown in Fig. 1. For investigating the structural vibration characteristics of the rolling-element bearing, a model of bearing assembly was considered a nonlinear spring-mass damper system. Elastic deformation between races and rollers gives a nonlinear force deformation relation, which is produced by Hertzian theory. In the mathematical modeling, the rolling-element bearing was considered a spring-mass system, and rolling elements acted as a nonlinear contact spring, as shown in Fig. 2. Since the Hertzian forces arose only when there was contact deformation, the springs were only required to act in compression. In other words, the respective spring force comes into play when the instantaneous spring length is shorter than its unstressed length; otherwise, balls and the races separate, and the resultant force is set to zero.

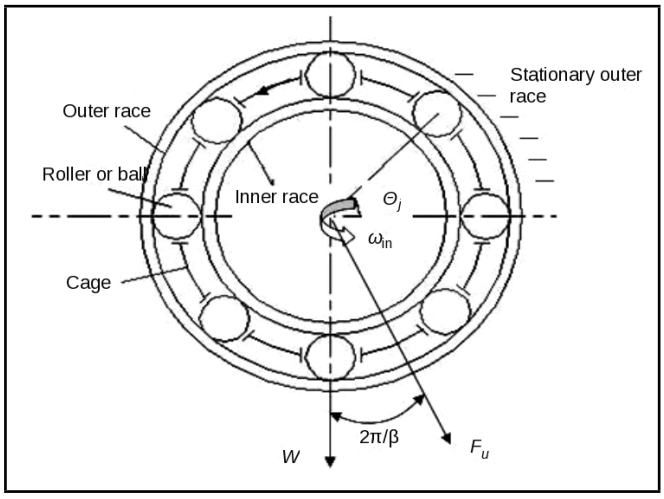

Figure 1. Schematic diagram of rolling-element bearings.

2.1. Ball Diameter Variations

When there is an off-sized ball in a bearing, this ball causes an additional deflection difference. This difference could be larger or smaller than the rest, depending on the off-sized ball diameter. Figure 3 shows that one ball has a greater diameter than the rest of balls in the set. This ball was forced to squeeze more in relation to the other balls and, hence, produced a greater force than the rest. Hence, for this off-sized ball, the equation of displacement of the j^{th} ball became (assuming the inner and outer races were rigid)

$$\delta\theta = \delta\theta_i + \Delta\Gamma, \tag{1}$$

where $\Delta\Gamma$ was the diameter difference of the off-sized ball. Because of the different ball diameters, the race was deformed into a complex shape that turned with the rotational speed of the cage.

2.2. Contact Stiffness

Hertz considered the stress and deformation in the perfectly smooth, ellipsoidal, and contacting elastic solids. Applying the classical theory of elasticity to the problem formed the basis of the stress calculation for machine elements as ball and roller bearings. Therefore, the point contact between the race and the ball developed into an area contact that had the shape

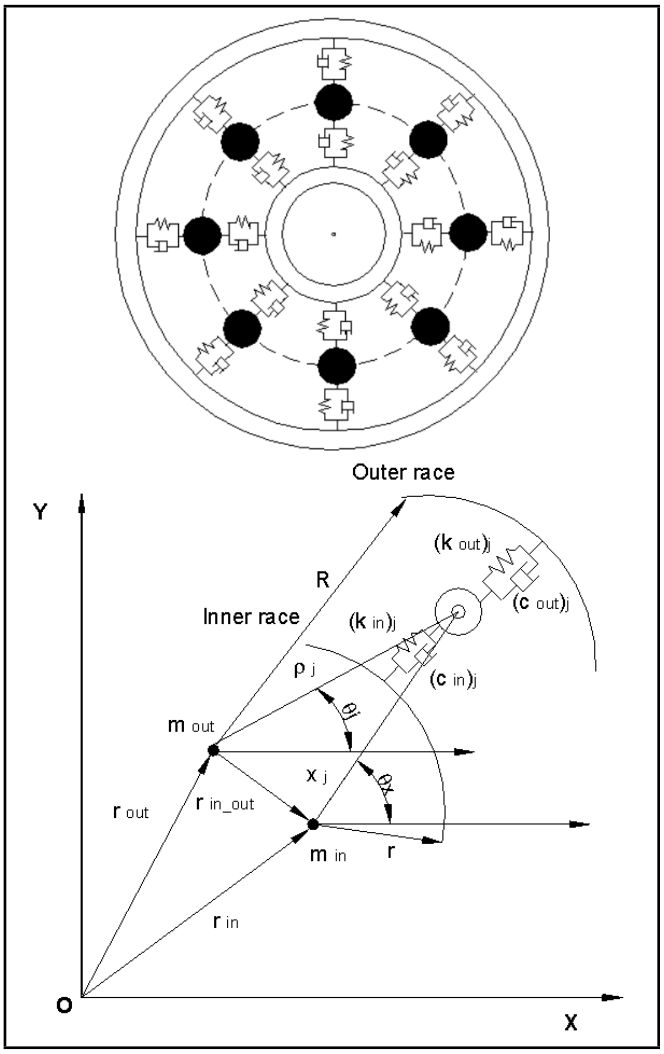

Figure 2. Mass-spring damper model of rolling-element bearings.

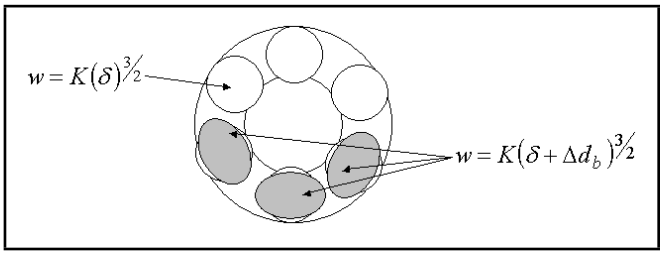

Figure 3. Presence of an off-sized ball in a ball set.

of an ellipse with a and b as the semi-major and semi-minor axes, respectively. It was assumed that the principal planes of curvature of the two bodies were concurrent; this is always the case for rolling-element bearings because the curvatures ρ_{11} and ρ_{21}, as well as ρ_{12} and ρ_{22}, lie in a common plane. The detailed description of the elastic modulus for the contact of a ball with the inner and outer race was already derived in paper;[12] the authors of this paper are using the same description.

2.3. Energy Expression of the Rolling-Element Bearings

The total energy of the system was considered to be the sum of kinetic energy, potential energy, strain energy of the springs representing contact, and dissipation energy due to contact damping. The detailed description of the energy expressions resulting from different parts of rolling bearings, which were already derived in the papers published by Harsha, were used in this paper.[10,11] The contacts between rolling elements and races were treated as nonlinear springs, which became stiff as a result of the Hertzian theory of elasticity. The nonlinear stiffness resulted from Hertzian contact effects and was evaluated by equations, which are given in Appendix A. In those previous papers, a constant damping value was chosen, but, for this paper, a nonlinear viscous damping model was adopted.

Energy dissipation

The lubrication was assumed to behave in a Newtonian way. Hence, a viscous damping model in which the dissipative forces were proportional to the time derivate of the mutual approach was adopted. The resulting equation yields

$$F_d = c(\delta)\,\dot{\delta}^q, \tag{2}$$

where $c(\delta)$ is also a function of the contact geometry, the material properties of the elastic bodies, the properties of lubricant, and the contact-surface velocities. Hence, the total-energy dissipation can be calculated, which is given in Appendix B.

2.4. Equations of Motion

The kinetic energy and potential energy contributed by the inner race, outer race, balls, rotor, and springs, could be differentiated with respect to the generalized coordinates ρ_j, $j = 1, 2, \ldots, N_b$, x_{in}, and y_{in} to obtain the equations of motion. For the generalized coordinates ρ_j, where $j = 1, 2, \ldots, N_b$, the equations were

$$\begin{aligned}
&\ddot{\rho}_j + g\sin\theta_j + \rho_j\dot{\theta}^2 - \frac{1}{m_j}\left(k_{\text{in_contact}}\right)\left[\delta_{\text{in}}\right]_+^{3/2}\frac{\partial\chi_j}{\partial\rho_j} \\
&\quad + \frac{1}{m_j}\left(k_{\text{out_contact}}\right)\left[\delta_{\text{out}}\right]_+^{3/2} \\
&\quad + \frac{1}{2m_j}\frac{\partial\left[\left(k_{\text{in_contact}}\right)\left(\left[\delta_{\text{in}}\right]_+^{1/2}\right)\right]}{\partial\rho_j}\left[\delta_{\text{in}}\right]_+^2 \\
&\quad + \frac{1}{2m_j}\frac{\partial\left[\left(k_{\text{out_contact}}\right)\left(\left[\delta_{\text{out}}\right]_+^{1/2}\right)\right]}{\partial\rho_j}\left[\delta_{\text{out}}\right]_+^2 \\
&\quad + \frac{3}{2m_j}\sum_{j=1}^{N_{r.e.}}\left\{c_{\text{in}}\left(k_{\text{in_contact}}\right)\delta_{\text{in}_+}^{3/2}\left(-\chi_j\right)^q\frac{\partial\chi_j}{\partial\dot{\rho}_j}\right\} \\
&\quad + \frac{3}{2m_j}\sum_{j=1}^{N_{r.e.}}c_{\text{out}}\left(k_{\text{out_contact}}\right)\delta_{\text{out}_+}^{3/2}\left(-\dot{\rho}_j\right)^q = 0 \\
&\qquad\qquad j = 1, 2, \ldots N_{r.e.}.
\end{aligned} \tag{3}$$

For the generalized coordinate x_{in} the equation was

$$\ddot{x}_{\text{in}} - \frac{1}{m_{\text{rotation}}} \sum_{j=1}^{N_{r.e.}} \left(k_{\text{in\_contact}}\right) \left[\delta_{\text{in}}\right]_{+}^{3/2} \frac{\partial \chi_j}{\partial x_{\text{in}}} + \frac{3}{2m_{\text{rotation}}} \sum_{j=1}^{N_{r.e.}} \left\{ c_{\text{in}} \left(k_{\text{in\_contact}}\right) \delta_{\text{in}_+}^{3/2} \left(-\dot{\chi}_j\right)^q \frac{\partial \dot{\chi}_j}{\partial \dot{x}_{\text{in}}} \right\} = \frac{F_u \sin(\omega_s t)}{m_{\text{rotation}}}. \quad (4)$$

For the generalized coordinate y_{in} the equation was

$$\ddot{y}_{\text{in}} + g - \frac{1}{m_{\text{rotation}}} \sum_{j=1}^{N_{r.e.}} \left(k_{\text{in\_contact}}\right) \left[\delta_{\text{in}}\right]_{+}^{3/2} \frac{\partial \chi_j}{\partial y_{\text{in}}} + \frac{3}{2m_{\text{rotation}}} \sum_{j=1}^{N_{r.e.}} \left\{ c_{\text{in}} \left(k_{\text{in\_contact}}\right) \delta_{\text{in}_+}^{3/2} \left(-\dot{\chi}_j\right)^q \frac{\partial \dot{\chi}_j}{\partial \dot{y}_{\text{in}}} \right\} = \frac{(W + F_u \cos(\omega_s t))}{m_{\text{rotation}}}, \quad (5)$$

where $m_{\text{rotation}} = (m_{\text{inner}} + m_{\text{rotor}})$.

This was a system of $(N_b + 2)$ non-linear differential equations. There was no external radial force allowed to act on the bearing system and no external mass attached to the outer race. The "+" sign as subscript in these equations signified that if the expression inside the bracket was greater than zero, then the rolling element at angular location θ_j was loaded giving rise to a restoring force, and if the expression inside the bracket was negative or zero, then the rolling element was not in the load zone, and the restoring force was set to zero.

3. METHODS OF SOLUTION

The nonlinear, second-order differential equations were solved by numerical integration, which is a time-domain approach. The non-analytic nature of the stiffness term rendered the system equations difficult for analytical solution.

3.1. Numerical Integration

The equations of motion, Eqs. (3), 4, and (5) were solved using the modified Newmark-β method to obtain the radial displacement, velocity, and acceleration of the rolling elements. To observe the nonlinear behavior of the system, parameters of the ball-bearings were selected and are given in Table 1. These bearings can operate at high speed without introducing much frictional effect; hence, they were suitable for high-speed applications (i.e., speeds greater than 5000 rpm). The ball-bearing 6002 was used for this study. The time step for the investigation was taken as $\Delta t = 10^{-5}$ sec.

3.2. Power Spectra, Poincaré Maps, and Lyapunov Exponent

Aperiodic behavior in a deterministic dynamical system was characterized by broadband frequency spectra. In sub-synchronous frequencies, the significant energy showed the aperiodic nature of the response. Poincaré maps were produced by plotting one of the system variables, e.g., the vertical or horizontal displacement against its derivative, once per rotational periodic of the system. For a synchronous limit cycle, a single point in the plane was repeated every cycle, while nth sub-harmonic was revealed by n and only n-repeated points. The Lyapunov exponent is a quantitative measure of the divergence properties of initially infinitesimally close attractor trajectories in the phase space. To calculate the Lyapunov exponent λ, two infinitesimally close points on an attractor were chosen. The trajectories that passed through these points were initially separated by a distance ε_0. After time t, the two points were separated by a distance ε_1, as discussed by Wolf et al.[13] It was measured in bits per second. A positive Lyapunov exponent indicates that $\varepsilon_t > \varepsilon_0$ (i.e., that the trajectories are diverging and that the system is chaotic). The Lyapunov exponent (λ) for the system is defined as

$$\lambda = \lim \left[\frac{1}{t} \log_2 \left(\frac{\varepsilon_t}{\varepsilon_0} \right) \right]. \quad (6)$$

4. RESULTS AND DISCUSSION

4.1. Ball-Size Variation is 0.2 μm

Because of the different ball diameters, the race was deformed into a complex shape that turns with the rotational speed of the cage. The off-sized balls were located symmetrically in bearings, such that they moved in the same direction simultaneously (i.e., the balls were assumed to be in phase). First, two balls assumed to be 0.2 μm oversized were taken. The responses were obtained for the bearing with varying ball size and for varying the speed of an unbalanced rotor. The ball set rotated at the cage speed around the inner race and the oversized ball. Since the ball set comes to the same position after one cage rotation, the system shows vibrations at a frequency that is equal to the number of balls multiplied by the cage speed $N_b\omega_{\text{cage}}$, i.e., at the system excitation frequency, i.e., at varying compliance frequency $(N_b\omega_{\text{cage}} = VC)$. The overall response plot of the rolling-element bearing for point contact with internal radial clearance 10 μm, radial load of 6 *N*, and unbalanced forces of 15% is shown in Fig. 4. To simplify the study, constant unbalanced force was assumed for the entire speed range. The overall response plots were generated for the combination of radial internal clearance, off-sized balls, and unbalanced force and have a high rough appearance.

The observed nature of response is 1T stable with a low amplitude of vibration up-to a shaft speed 450 rpm, which is confirmed by a negative value of the Lyapunov exponent ($\lambda < 0$), as shown in Fig. 5. When the speed of the rotor increases the period, one solution becomes multi-orbit unstable from 500 to 2350 rpm because of periodic doubling bifurcations. The Eigen values of the monodromy matrix go out through -1, and also the value of the Lyapunov exponent varies in between 0 to 0.45, i.e., $\lambda > 0$. The solution undergoes pitchfork bifurcation until 2350 rpm, after which the chaotic solution is

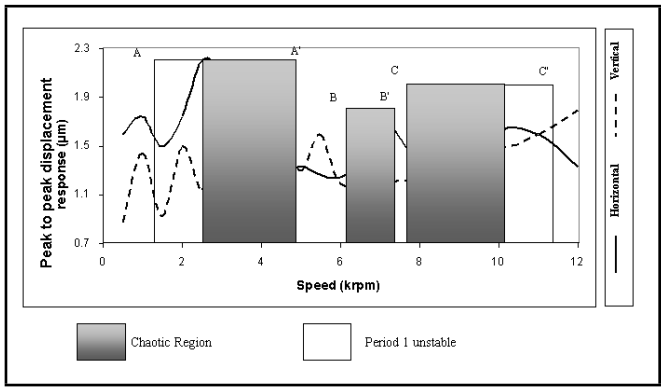

Figure 4. Speed-response plot for ball-size variation of unbalanced rotor.

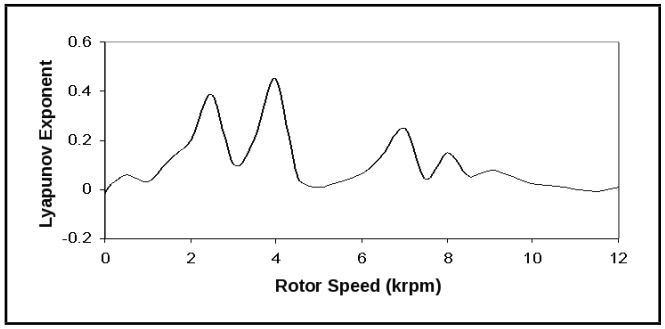

Figure 5. Lyapunov exponent.

obtained at 2500 rpm. The nature of the solution at 2500 rpm is observed as the onset of chaos with super-harmonic character of frequency spectra, as shown in Fig. 6. The dense band of frequency spectrum shows the presence of both the rotational frequency ($X = 41.66$ Hz) and the varying compliance frequency ($VC = 8\omega_{\text{cage}} = 133.33$ Hz). The presence of dense regions in the orbit is indicative of the onset of chaos. It cannot be considered perfectly periodic, since the two are not exactly line spectra. The peak amplitude of vibration appeared in the spectrum at the varying compliance frequency ($VC = 8\omega_{\text{cage}} = 133.33$ Hz) and rotational frequency ($X/2 = 20.83$ Hz), as shown in Fig. 6. Other major peaks at super harmonics of vibration appear at $VC + X/2 = 154.16$ Hz, $VC + \omega_{\text{cage}} = 149.99$ Hz, $2VC + X = 308.32$ Hz, $3VC = 400$ Hz and $3VC + 4\omega_{\text{cage}} = 466.64$ Hz.

The first chaotic region appeared between 2500 to 4250 rpm; the loss of stability could be seen to be by the Eigen value crossing $+1$. The chaotic solutions at 2500 and 4100 rpm are shown in Figs. 6 and 7, respectively. The frequency spectrum had a broadband structure, as seen in between spikes of VC, $X/2$, and their multiples. The Lyapunov exponent had a high positive value in this region ($\lambda > 0$), which confirms the chaotic nature of system, as shown in Fig. 5. The vibration spectrum shows the interaction between both the frequency components that produce sum and difference combination frequencies. It is clear that a loss of periodicity is a characteristic feature of a chaotic solution. As the speed increases, the system showed quasi-periodic behavior. The second chaotic region appeared in between the speed range of 6000 to 6950 rpm. The system showed onset of chaos when the rotor speed

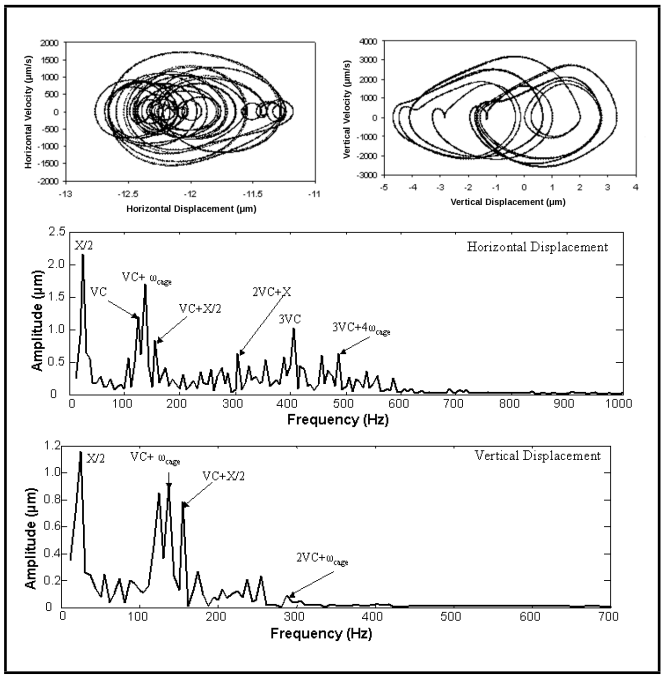

Figure 6. Poincaré map and FFT of unbalanced rotor at speed 2500 rpm for ball-size variation 0.2 μm.

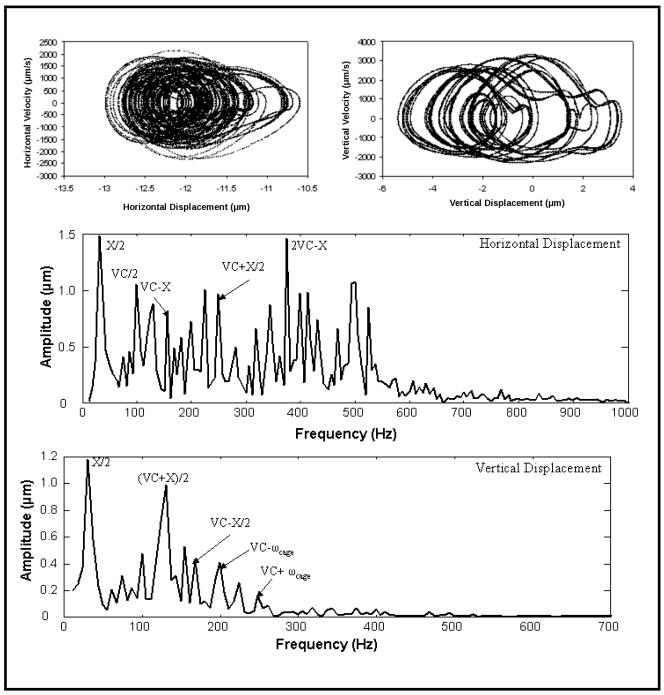

Figure 7. Poincaré map and FFT of unbalanced rotor at speed 4100 rpm for ball-size variation 0.2 μm.

is 6000 rpm, as shown in Fig. 8. For rotor speed 6000 rpm, the peak amplitude appears in the vibration spectra at the rotational frequency $X/2 = 50$ Hz and at $7VC/5 = 448$ Hz, as shown in Fig.8. Other major peaks at super-harmonics of vibration appear at $VC = 8\omega_{\text{cage}} = 320$ Hz, $VC + X = 420$ Hz, $VC - X = 220$ Hz, $VC + 2X = 520$ Hz, $VC + \omega_{\text{cage}} = 360$ Hz and $VC - \omega_{\text{cage}} = 280$ Hz.

When the speed of the unbalanced rotor was 6900 rpm, the dense frequency spectrum observed during the peak amplitude of vibration appears at the rotational frequency $X/2 = 57.5$ Hz

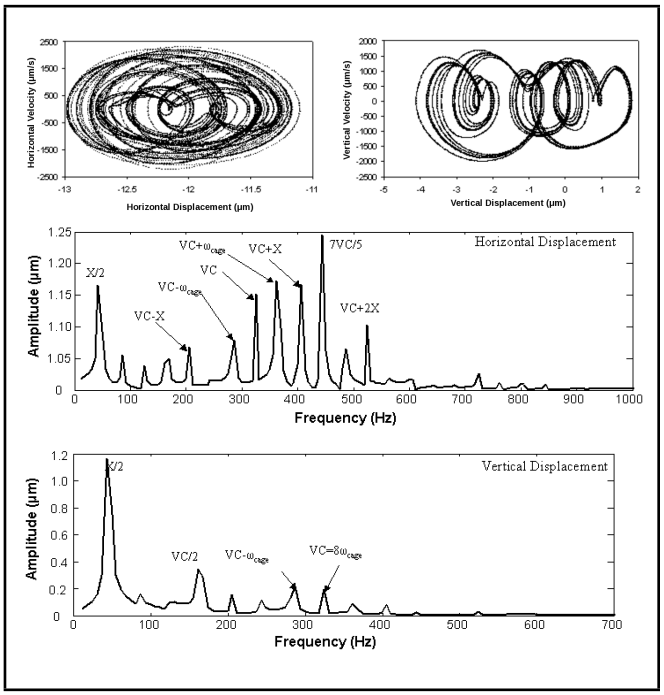

Figure 8. Poincaré map and FFT of unbalanced rotor at speed 6000 rpm for ball-size variation 0.2 μm.

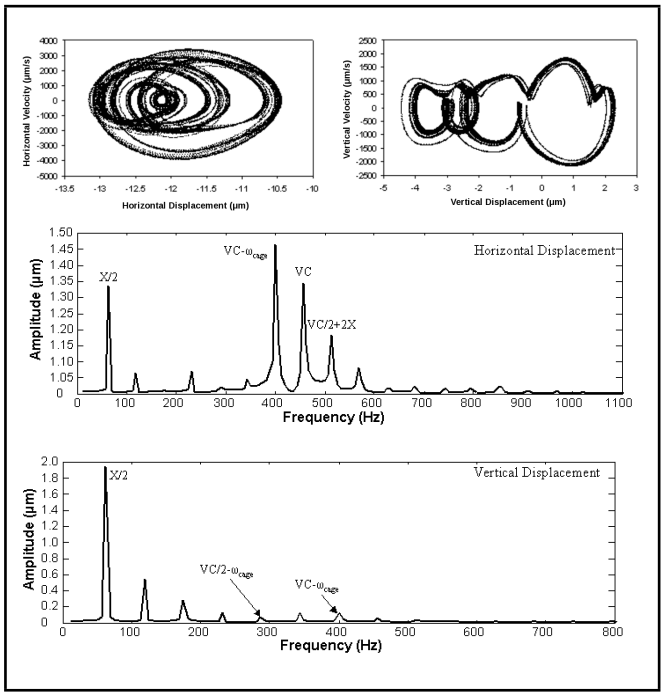

Figure 10. Poincaré map and FFT of unbalanced rotor at speed 8500 rpm for ball-size variation 0.2 μm.

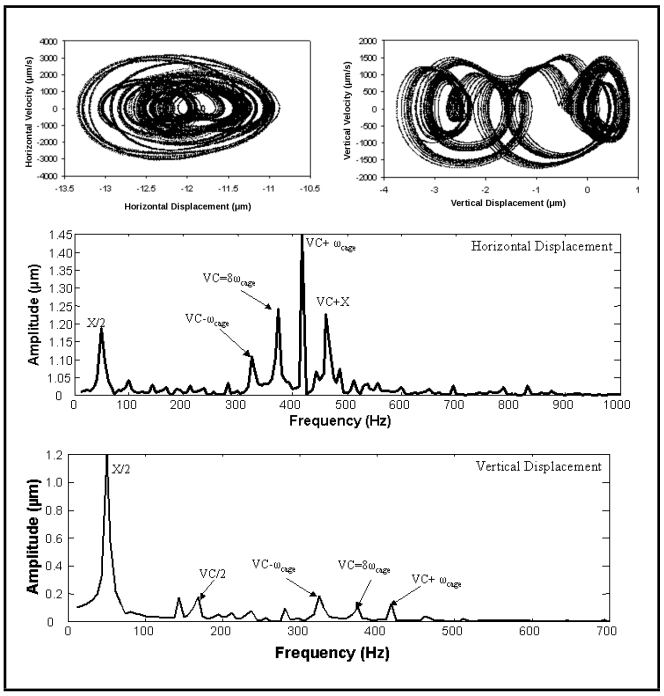

Figure 9. Poincaré map and FFT of unbalanced rotor at speed 6900 rpm for ball-size variation 0.2 μm.

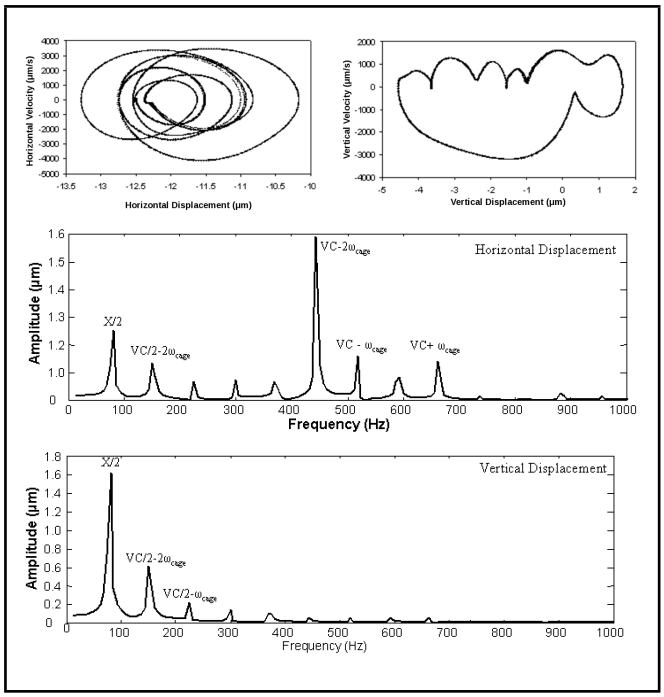

Figure 11. Poincaré map and FFT of unbalanced rotor at speed 11000 rpm for ball-size variation 0.2 μm.

and at $VC + \omega_{\text{cage}} = 414$ Hz, as shown in Fig. 9. Other major peaks of vibration amplitude appear at $VC = 8\omega_{\text{cage}} = 368$ Hz, $VC - \omega_{\text{cage}} = 322$ Hz, $VC + \omega_{\text{cage}} = 414$ Hz, and $VC + X = 483$ Hz. The frequency spectra for chaotic nature are broadband, which may have spikes at particular excited frequencies. A chaotic solution of the system is also confirmed by variation in the positive value of the Lyapunov exponent ($\lambda > 0$), as shown in Fig. 5. The Poincaré map of a chaotic solution has a fractal structure, which repeats itself as the map is magnified. Loss of periodicity is clearly seen, which is a well-known characteristic of chaotic response.

The low-amplitude region of the unstable-period solution started from 7500 rpm and extended up to 9500 rpm. For the third chaotic region between 7600 rpm to 10000 rpm, the loss of stability was seen when the Eigen value crossed $+1$. In Fig. 10, the chaotic response at 8500 rpm is shown by the band structure of frequencies in frequency spectra. These band structures developed around $X/2$ in the vertical and in the entire speed range for the horizontal displacement. The fine-layered structure of the strange attractor is also clear from

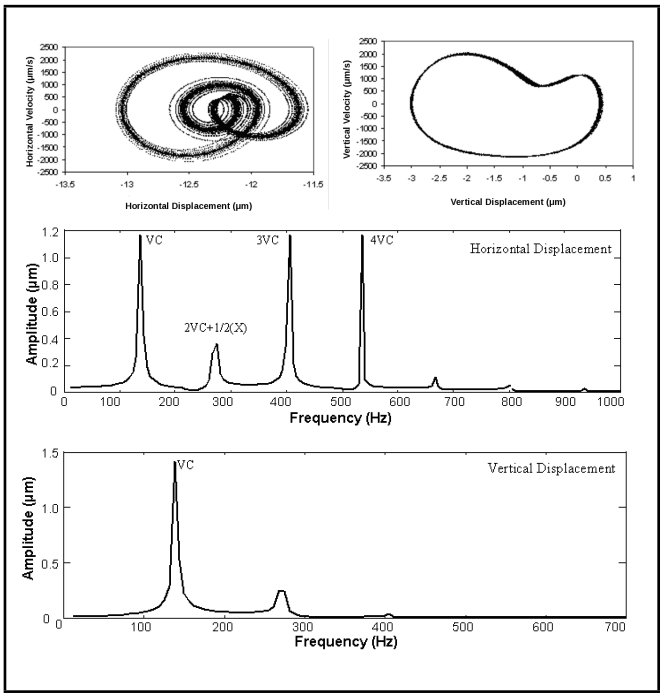

Figure 12. Poincaré map and FFT of unbalanced rotor at speed 2500 rpm for ball-size variation 2 μm.

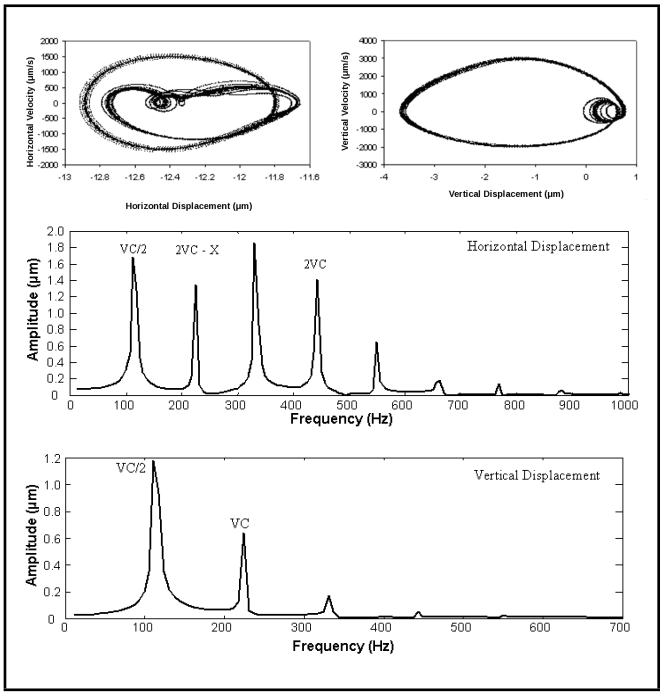

Figure 13. Poincaré map and FFT of unbalanced rotor at speed 4100 rpm for ball-size variation 2 μm.

the Poincaré maps. The presence of dense regions in the orbit is indicative of chaos. Again as the speed increases, the system shows quasi-periodic behavior. For this speed, the region value of the Lyapunov exponent varied nearly to zero, which confirms the quasi-periodic behavior of the system. As speed increases to 11000 rpm, system stability returned, and system shows a periodic nature, as shown in Fig. 11.

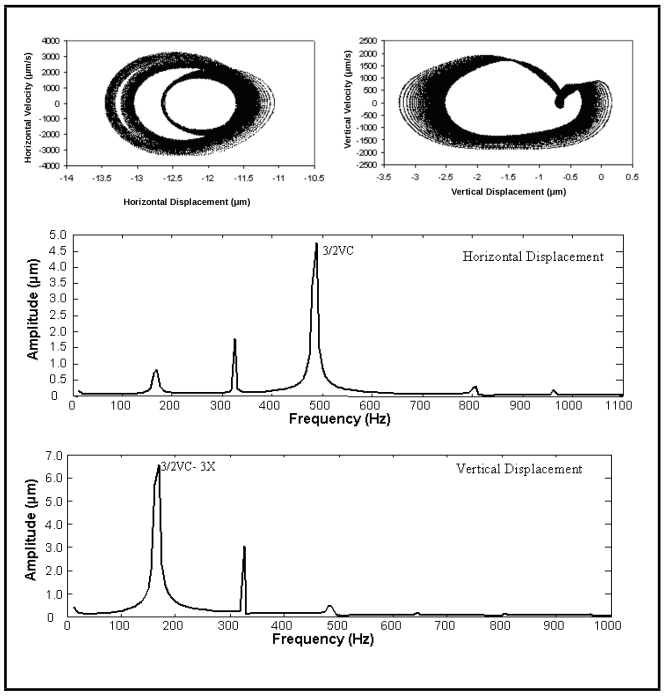

Figure 14. Poincaré map and FFT of unbalanced rotor at speed 6000 rpm for ball-size variation 2 μm.

4.2. Ball-Size Variation is 2 μm

The off-sized balls were located symmetrically in bearings in such a way that they moved in the same direction simultaneously (i.e., the balls were assumed to be in phase). First, two balls that were assumed to be 2 μ*m* oversized were taken. The responses were obtained for the bearing with varying ball size and for varying the speed of unbalanced rotor.

The nature of the solution at 2500 rpm was observed as the onset of chaos with multiple excitation peaks of frequency spectra, as shown in Fig. 12. The frequency spectrum shows the presence of both the rotational frequency (X) and the varying compliance frequency (VC). The presence of dense regions in the orbit is indicative of the onset of chaos. It could be considered perfectly periodic, since the two were not exactly line spectra. The nature of solutions at 4100 rpm shows the chaos with a weak attractor, as shown in Fig. 13. The frequency spectrum shows the spikes of VC, $X/2$, and their multiples. When the speed of the unbalanced rotor is 6000 rpm, the dense-frequency spectrum observed with the peak amplitude of vibration appears at the interaction between varying compliance frequency and rotational frequency as at $3/2VC + 3X$, which is shown in Fig. 14. The Poincaré map of a chaotic solution has a fractal structure, which repeats itself as the map is magnified in Fig. 14. A loss of periodicity is clearly seen, which is a well-known characteristic of chaotic response. When the speed is increased to 6900 rpm, the system shows a chaotic nature with a weak attractor and peak excitation appearing at VC and at X, along with their interactions, as shown in Fig. 15.

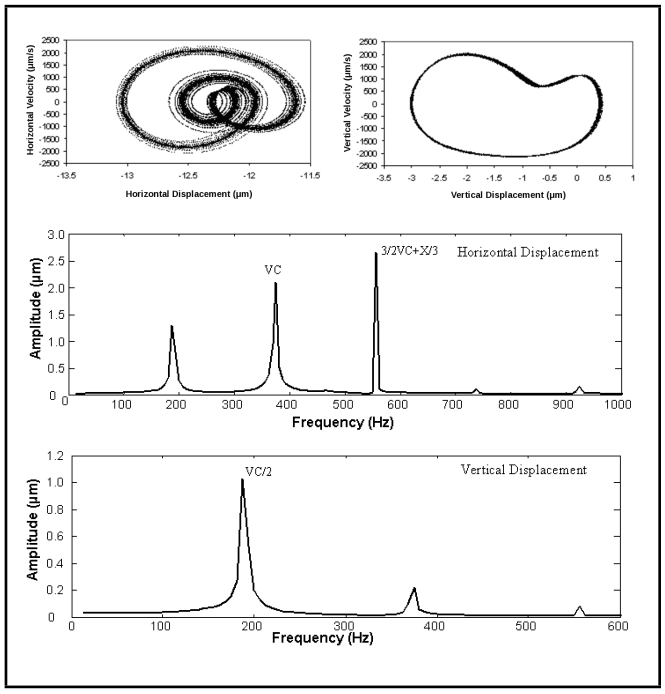

Figure 15. Poincaré map and FFT of unbalanced rotor at speed 6900 rpm for ball-size variation 2 μm.

5. CONCLUSION

In the present investigation, a mathematical model of a rotor-bearing system was developed to observe the nonlinear response of an unbalanced rotor due to ball-size variations. Two cases of ball-size variation were considered: variations of 0.2 micron and 2 microns. Using this model, the vibration response of the bearing was demonstrated to be chaotic for some specific combinations of nonlinear stiffness, nonlinear damping, and rotational speed combined with off-sized rolling elements to provide sufficient nonlinearity. For cases that were stable during free motion and not close to the neutral-stability line, a limited range of chaos could be detected. The route to chaos was observed to be an intermittency mechanism by period-doubling behavior. Frequency spectra displayed multiples of $1X$ and VC as well as the linear combination of the two frequencies. From the obtained response, the following conclusions are drawn:

- In the case of ball-size variation, symmetric combinations will produce vibrations at the multiple of the cage speed. A single off-sized ball within a bearing produces vibrations at the cage speed. This is true for linear and nonlinear ball-to-race deflection coefficients. The highest radial vibrations caused by ball-size variation are at a speed of the number of balls multiplied by the cage speed ($\omega = k\omega_{\text{cage}}$ Hz). The other vibrations due to ball-size variation also occur at $VC \pm k\omega_{\text{cage}}$, where k is a constant. From this analysis, a prediction can be made about the major peaks at frequencies for off-sized balls, and the model predicts discrete spectra having significant components at multiples of cage frequency.

- Nonlinear dynamic responses are found to be associated with rotational frequency. From the obtained responses, it can be inferred that a speed with an unbalanced force in the set will produce nonlinear vibrations at the rotational frequency of the ball (X). Other major peaks also appear at the combination of two exciting frequencies such as $VC + X$.

Table 1. Geometric and physical properties used for the ball bearings.

Ball radius	4.762 mm
Inner Race Diameter	18.738 mm
Outer Race Diameter	28.262 mm
Internal radial clearance	10 μm
Radial load	6 N
Mass of rotor	0.6 kg
Pitch radius of the ball set	27 mm
Ball diameter variation	0.2 μm, 2 μm
Unbalanced rotor force	15 %
No. of rolling elements	08

- The rotor-bearing system has three high-amplitude regions. The first region is one of periodic doubling response where the period-one response is unstable. Chaotic responses appear in this region, which has a strong attractor compared to the chaotic behavior in other regions. The second region shows a chaotic nature with a weak attractor, and it also exists for a short speed range. The third region has a maximum p-p value, and this region has an unstable response due to Hopf bifurcation generating amplitude modulation and quasi-periodic response. The ratio of the carrier frequency (VC) to the modulating frequency decreases as the speed is increased. This leads to quasi-periodic and mode-locked behavior.

REFERENCES

[1] Tallian, T. E. and Gustafsson, O. G. Progress in Rolling Bearing Vibration Research and Control, *ASLE Trans*., **8**, 195–207, (1965).

[2] Meyer, L. D., Ahlgren, F. F., and Weichbrodt, B. An Analytic Model for Ball Bearing Vibrations to Predict Vibration Response to Distributed Defects, *ASME J. Mech. Des*., **102**, 205–210, (1980).

[3] Wardle, F. P. and Poon, S. Y. Rolling Bearing Noise — Cause and Cure, *CME*, 36–40, (1983)

[4] Sunnersjo, C. S. Rolling Bearing Vibrations — Geometrical Imperfections and Wear, *Journal of Sound & Vibration*, **98**, 455–474, (1985).

[5] Gustafson, O. G., Tallian, T., Gad, E. H. and Fukata, S. Research report on study of the vibration characteristics of bearings report: AL 631 023, *SKF Ind. Inc,* Reg: 585, **14**: 4223, (1963).

[6] Meyer, L. D., Ahlgran, F. F. and Weichbrodt, B. An analytical model for ball bearing vibrations to predict vibration response to distributed defects. *ASME J. Mech. Des*, **102**, 205–210, (1980).

[7] Gad, E. H., Fukata, S. and Tumara, H. Computer simulation of rotor radial vibration due to ball bearings. *Mem. Fac. Engng, Kyushu Univ.,* **44**(1), 83–111, (1984).

[8] Aktürk, N. Some characteristic parameters affecting the natural frequency of a rotating shaft supported by defect-free ball bearings. *Proc. Instn Mech. Engrs,* **217,** *Part K: J. Multi-body Dynamics,* 145-151, (2003).

[9] Harsha, S. P., Sandeep, K. and Prakash, R. Effects of preload and number of balls on nonlinear dynamic behaviors of ball bearing system. *Int. J. Nonlinear Sci. Numer. Simul,* **4**(3), 265–278, (2003).

[10] Harsha, S. P. Non-linear dynamic responses of a balanced rotor supported by rolling element bearings due to radial internal clearance effect, *Mechanism and Machine Theory,* **41**, 688-706, (2006).

[11] Harsha, S. P. Non-linear dynamic analysis of high speed rotor supported by rolling element bearings, *Journal of sound and vibration,* **290**, 65–100, (2006).

[12] Upadhyay S. H., Jain S. C. and Harsha S. P. Chaos and Nonlinear Dynamic Analysis of High-Speed Rolling Element Bearings due to Varying Number of Rolling Elements. *Int. J. Nonlinear Science Numerical Simuationl,* **10**(3), 323–332, (2009).

[13] Wolf A, Swift J. B, Swinney, H. L. and Vastano, J. A. Determining Lyapunov exponents from a time series. *Physica D*, **16**: 285–317, (1985).

[14] Harris, T. A. *Rolling Bearing Analysis*, Wiley, New York, (2001).

[15] Krämer, E. *Dynamics of rotors and foundations,* New York: Springer, (1993).

[16] Bathe, K. and Wilson, E. *Numerical methods in finite element analysis,* Englewood Cliffs, NJ: Prentice-Hall, (1990).

APPENDIX A. CONTACT DEFORMATION

For pure-point contact, the potential energy related to the contact is calculated from the theory of Hertzian contact deformation; the relationships for a point contact in ball bearings is an expression of a force with the displacement raised to an exponent (q).[14] Where

$$k_{\text{in}} \int_0^{\delta_{\text{in}}} \left(\left(k_{\text{in\_contact}} \right) \delta_{\text{in}}^{q} \right) d_f, \tag{A.1}$$

$$k_{\text{in}} = \frac{1}{q+1} k_{\text{in\_contact}} \delta_{\text{in+}}^{q+1}, \tag{A.2}$$

now the generalized part of potential energy is

$$\frac{1}{q+1} k_{\text{in\_contact}} \delta_{\text{in+}}^{q+1} = \frac{1}{q+1} k_{\text{in}} \delta_{\text{in+}}^{2}. \tag{A.3}$$

Hence, ball-bearing ($q = 3/2$) stiffness at inner and outer race is

$$k_{\text{in}} = k_{\text{in\_contact}} \sqrt{\delta_{\text{in+}}}, \tag{A.4}$$

$$k_{\text{out}} = k_{\text{out\_contact}} \sqrt{\delta_{\text{out+}}}. \tag{A.5}$$

APPENDIX B. CONTACT DAMPING

For the j^{th} rolling element the equivalent contact stiffness between the rolling element and race is

$$k_{\text{Eq}} = \frac{3}{2} k_{\text{contact}} \delta^{\frac{1}{2}}. \tag{B.1}$$

The deforming forces for the j^{th} rolling element and inner race is

$$F_{\text{d\_in}} = c_{\text{in}} k_{\text{Eq}} \left(\dot{\delta_{\text{in}}} \right)_{+}^{q}, \tag{B.2}$$

$$F_{\text{d\_in}} = \frac{3}{2} c_{\text{in}} \left(k_{\text{in\_contact}} \right) \delta_{\text{in+}}^{\frac{1}{2}} \dot{\delta}_{\text{in+}}^{q}.^{15} \tag{B.3}$$

Similarly, the damping force for the j^{th} rolling element with the outer race is

$$F_{\text{d\_out}} = c_{\text{out}} \delta_{\text{out+}} k_{\text{eq}}, \tag{B.4}$$

$$F_{\text{d\_out}} = \frac{3}{2} c_{\text{out}} \left(k_{\text{out\_contact}} \right) \delta_{\text{out+}}^{\frac{1}{2}} \dot{\delta}_{\text{out+}}^{q}. \tag{B.5}$$

Hence, the total energy dissipation at both contact points of the rolling element with the inner and outer race is

$$E_{\text{dissipation}} = \frac{3}{2\left(q+1\right)} \sum_{j=1}^{N_{\text{r.e.}}} \left[\left\{ c_{\text{in}} \left(k_{\text{in\_contact}} \right) \delta_{\text{in+}}^{\frac{3}{2}} \dot{\delta}_{\text{in+}}^{q+1} \right\} + \left\{ c_{\text{out}} \left(k_{\text{out\_contact}} \right) \delta_{\text{out+}}^{\frac{3}{2}} \dot{\delta}_{\text{out+}}^{q+1} \right\} \right]. \tag{B.6}$$